Monolithic route to efficient dye-sensitized solar cells employing diblock copolymers for mesoporous TiO_2†‡

Mihaela Nedelcu,§¶[ab] Stefan Guldin,¶[ab] M. Christopher Orilall,||[c] Jinwoo Lee,[c] Sven Hüttner,[ab] Edward J. W. Crossland,[abd] Scott C. Warren,††[c] Caterina Ducati,[e] Pete R. Laity,[e] Dominik Eder,[e] Ulrich Wiesner,[c] Ullrich Steiner[abd] and Henry J. Snaith*[f]**

Received 28th September 2009, Accepted 24th November 2009
First published as an Advance Article on the web 23rd December 2009
DOI: 10.1039/b920077k

We present a material and device based study on the fabrication of mesoporous TiO_2 and its integration into dye-sensitized solar cells. Poly(isoprene-*block*-ethyleneoxide) (PI-*b*-PEO) copolymers were used as structure directing agents for the sol–gel based synthesis of nanoporous monolithic TiO_2 which was subsequently ground down to small particles and processed into a paste. The TiO_2 synthesis and the formation of tens of micrometre thick films from the paste is a scalable approach for the manufacture of dye sensitised solar cells (DSCs). In this study, we followed the self-assembly of the material through the various processing stages of DSC manufacture. Since this approach enables high annealing temperatures while maintaining porosity, excellent crystallinity was achieved. Internal TiO_2 structures ranging from the nanometre to micrometre scale combine a high internal surface area with the strong scattering of light, which results in high light absorption and an excellent full-sun power conversion efficiency of up to 6.4% in a robust, 3 μm thick dye-sensitized solar cell.

1 Introduction

Since the advent of the space race, an enormous amount of work has focused on developing highly efficient, durable photovoltaic technologies. Over recent years, with the realization of an impending fuel shortage and the need for clean, renewable sources of energy, considerable effort has been made to reduce the cost of solar cells by primarily addressing the material processing techniques and developing radical new approaches to photovoltaic technologies. Photo-electrochemical solar cells are an emerging photovoltaic technology which could revolutionize this industry. Dye-sensitized solar cells (DSCs), introduced by O'Regan and Grätzel in 1991,[1] are composed of a low-cost mesoporous n-type metal oxide, typically TiO_2. Sensitization of this oxide with dye molecules and subsequent in-filling with a redox-active liquid electrolyte and capping with a Pt counter electrode completes the device. Electrons are injected into the metal oxide following optical excitation of the dye. The redox active electrolyte regenerates the oxidized dye species with the holes carried back to the counter electrode to complete the circuit. Because light absorption occurs only in a monolayer of dye, an extremely large internal surface area is required to enable complete light absorption, typically 1000-fold compared to a planar geometry. This is usually achieved by forming mesoporous films from sol–gel processed sintered nanoparticles with a surface roughness of approximately 100-fold per micron thickness.[1–3] Achieving the correct pore structure and good interconnection between particles is likely to be critical to further improving the efficiency, reproducibility, and longevity of these solar cells. The mesoporous films fabricated from sol–gel processed nanoparticles have been remarkably successful. However, after twenty years of optimization, further improvements are not directly foreseeable.

Recently, approaches which make use of copolymer self-assembly to control the TiO_2 morphology on the 10 nm length scale have been reported. A block copolymer can, for example, be used as a sacrificial template. Selectively degrading one of the blocks and back-filling the remaining porous polymer template with the required material *via* electrochemical deposition, chemical vapor deposition or thermal deposition, and removal of

[a]*Department of Physics, Cavendish Laboratory, University of Cambridge, J. J. Thomson Avenue, Cambridge, CB3 0HE, UK*
[b]*The Nanoscience Center, Interdisciplinary Research Collaboration in Nanotechnology, University of Cambridge, 11 J. J. Thomson Avenue, Cambridge, CB3 0FF, UK*
[c]*Department of Materials Science and Engineering, Cornell University Ithaca, New York, 14853, USA*
[d]*Freiburg Institute for Advanced Studies, Albert-Ludwigs-Universität Freiburg (FRIAS), Albertstr. 19, 79104 Freiburg, Germany*
[e]*Department of Materials Science & Metallurgy, University of Cambridge, Cambridge, CB2 3QZ, UK*
[f]*Department of Physics, University of Oxford, OX1 3PU, UK. E-mail: hsnaith1@physics.ox.ac.uk*

† This paper is part of a *Journal of Materials Chemistry* issue highlighting the work of emerging investigators in materials chemistry.

‡ Electronic supplementary information (ESI) available: Solar cell performance of 30 μm thick film; transport and recombination; analysis of small-angle X-ray data; nitrogen physisorption. See DOI: 10.1039/b920077k

§ Current address: Department of Chemistry and Biochemistry, Ludwig-Maximilians-Universität München, Butenandstr. 11, 81377 München, Germany.
¶ These authors contributed equally to this work.
|| Current address: NRC Institute for Fuel Cell Innovation, 4250 Wesbrook Mall, Vancouver, B.C. V6T 1W5, Canada.
** Current address: Department of Chemical Engineering and School of Environmental Science and Engineering, Pohang University of Science and Technology, Kyungbuk, 790-784, Korea.
†† Current address: Ecole Polytechnique Federale de Lausanne, Laboratory of Photonics and Interfaces, 1015 Lausanne, Switzerland.

the sacrificial polymer results in the creation of a close to identical replica of the original block copolymer morphology.[4,5] A simpler approach is to use block copolymers as structure directing agents in a sol–gel process.[6–8] A metal-containing sol is incorporated into a copolymer morphology, which becomes selectively enriched in one of the copolymer microphases. The condensation reaction during solvent extraction and subsequent high temperature steps result in a mesostructured ceramic that closely mirrors the microphase morphology of the initial organic–inorganic hybrid.

The amphiphilic triblock copolymer poly(ethylene glycol-*block*-propylene glycol-*block*-ethylene glycol) (P123) has caught particular interest for the fabrication of highly efficient dye-sensitized solar cells with benefits of greatly enhanced control of pore size, uniformity, and interconnectivity.[9,10] However, the kinetics of mesoscopic structure equilibration in this system are slow (processing times up to several days) and high processing temperatures (up to 650 °C) can lead to the collapse of the mesostructure.[11] The requirement for high calcination temperatures can be bypassed to a certain extent by incorporating titania nanocrystals into the hybrid material.[12] As an alternative to P123, the block copolymer poly(isoprene-*block*-ethylene oxide) (PI-*b*-PEO) has attracted recent interest as it exhibits a significantly larger interaction parameter χ between the repelling blocks as well as a higher degree of polymerisation.[7,13,14] These properties drastically reduce the time for microphase separation and PI-*b*-PEO also offers larger pore sizes compared to P123, which enables the effective infiltration with functional material.[15] Recently, Lee *et al.* have introduced a new fabrication protocol, defined as a combined assembly by soft and hard (CASH) chemistries. Since in a first calcination step under inert environment the hydrophobic block is converted into a supporting carbonaceous scaffold, much higher crystallisation temperatures can be accessed.[8]

A long-standing limitation in the manufacture of sol–gel derived thick films is the build-up of high in-plane stresses during the calcination process leading to the formation of cracks and film delamination,[9,16] which restricts the commercial viability of these methods. By separating the calcination process from film deposition, the manufacture of thick efficient DSCs is feasible. This was recently demonstrated by Wei *et al.*[10] The mesoporous material is formed as a monolith which is ground into small particles. The subsequent formation of a paste incorporating these particles, a polymer and a binder makes the nanostructured materials applicable for a rapid, large-area coating. With this paste of preformed, precrystallized mesoporous particles of predetermined scale and morphology, up to 30 μm thick films can easily be deposited. Incorporating these films into liquid electrolyte dye-sensitized solar cells proves to be very effective.

The work presented here employs the CASH method to increase the TiO_2 annealing temperatures in order to better control the crystallinity of the mesoporous TiO_2. The detailed evolution of the copolymer-directed morphology of the materials from the precursor to the final device is studied and the multiple scattering of light within the photoactive layer is identified as one of the main contributions to the excellent device performance in relatively thin films (3.5 μm).

2 Results and discussion

2.1 Mesoporous material and thin film characterisation

Mesoporous titania was prepared as shown schematically in Fig. 1 and previously described in detail.[8,15] In short, a PI-*b*-PEO block copolymer with a molecular weight M_n = 33.5 kg mol^{-1}, polydispersity 1.1 and a PEO weight fraction of 0.23 was dissolved in anhydrous tetrahydrofuran (THF). $TiCl_4$ and Ti-isopropoxide were added and the solution was stirred for 2h. Following the evaporation of the solvent at 50 °C in air, the material was annealed to anatase TiO_2 at 525 °C in argon, followed by O_2. The resulting mesoporous monolith was ground to a powder and processed into a paste by solvent addition following a similar method to that of Ito *et al.*;[17] see experimental section for details.

The first part of our study concerns the evolution of the copolymer-directed morphology of the materials at various stages of the fabrication process as shown in Fig. 2. Upon solvent evaporation, the copolymer self-organises into a microphase morphology that is determined by the block copolymer architecture and by a relative swelling of the PEO domains by the titania sol. The TEM image in Fig. 2a suggests the formation of a micellar morphology consisting of close-packed PI micellar cores surrounded by a PEO/Ti-sol matrix. The SAXS data in Fig. 2d suggests a face-centred orthorhombic (f.c.o.) assembly of the micelles when compared to a respective fit of scattering bodies in f.c.o. configuration, shown in Fig. 2g. The structure is contracted (compared to the cubic symmetry) normal to the surface onto which the material was cast as a thick film.

The close-packed copolymer-directed micellar structure is preserved during annealing at 525 °C (Fig. 2b). The disappearance of the higher order peaks in the SAXS analysis in Fig. 2e

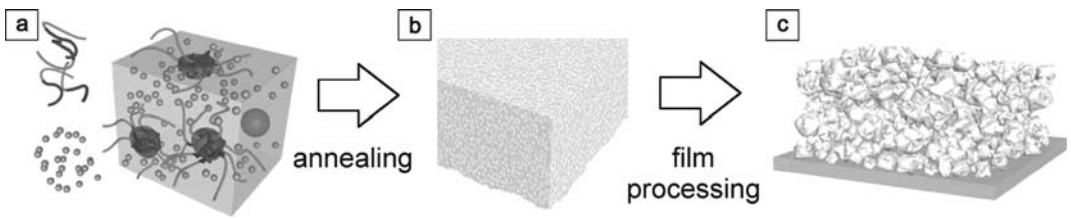

Fig. 1 Schematic of the material preparation process. (a) Solution of PI-*b*-PEO copolymer and TiO_2 precursors, where the titania precursors selectively swell the PEO phase. (b) An ordered, highly porous and crystalline TiO_2 network is revealed after the organic components are removed by high temperature treatments. (c) Assembly of the nanocrystals into a random network when a film is formed by doctor blading of a paste made from the ground powder.

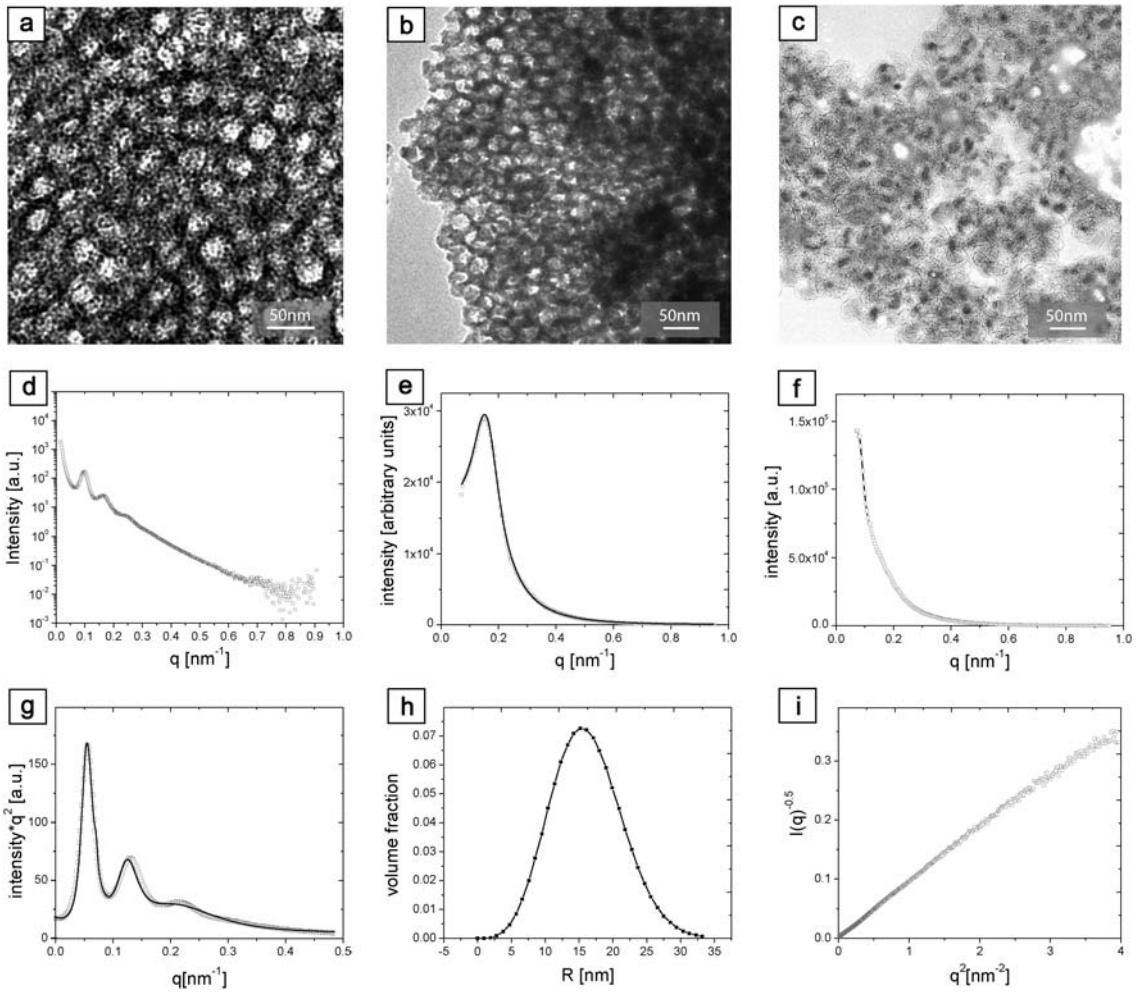

Fig. 2 (a)–(c) TEM images of the TiO_2 structure (a) before, (b) after high temperature treatment and (c) after paste processing. The evolution of the structure from an ordered micellar morphology in the monolith before grinding to a highly porous, yet disordered configuration in the actual TiO_2 film is confirmed by SAXS ((d)–(i)). In the second line integrated 2D SAXS patterns are shown of (d) hybrid bulk material, (e) annealed bulk material and (f) TiO_2 after paste processing and film deposition. Model fitting of data supports observed morphologies: (g) the hybrid material can be described by a micellar morphology in a face-centred-orthorhombic configuration. The first-order peak of the porous micellar network in (e) is maintained during annealing but the higher-order peaks are lost. The particle size distribution in (h) is derived from a fit of the data in (e) using a 'distorted lattice' model.[19] The absence of a scattering peak in (f) and the linear variation of the data in the Debye–Bueche plot of the paste processed material in (i) supports the assumption of a random network of TiO_2 nanocrystals with a characteristic structure size of 6.7 nm.

reveals, however, a loss in long-range order which is accompanied by a structural contraction, reducing the characteristic length scale from 64 nm to 43 nm. This is not surprising since both the removal of the organic structure directing agent and the crystallisation of the titania network lead to a significant volume contraction.[18] Fig. 2h shows the size distribution of scattering bodies in the calcined titania sample which is derived from a fit of the data in Fig. 2e using a "distorted lattice" model.[19] The further processing of the mesoporous anatase titania involved grinding-down the material in a mortar and sonication of the ethanol based paste to disperse the particles. This resulted in a destruction of the close packed morphology as witnessed in Fig. 2c which reveals a disordered assembly of nanocrystals. This is confirmed by the SAXS spectrum in Fig. 2f, which lacks a first-order peak in the expected q-range. The Debye–Bueche plot[20,21] of $I(q)^{-0.5}$ *vs.* q^2 in Fig. 2i supports the formation of a random network of TiO_2 nanocrystals. The characteristic mesh size of the disordered nanocrystal assembly of 6.7 nm is approximately 1/2 of the value of the crystallite size.

While grinding and sonication resulted in a significant change in the mesoscopic morphology, the intrinsic crystallinity of the material is unaffected, as shown in Fig. 3. High resolution transmission electron microscopy (HRTEM) of mesoporous TiO_2 before and after grinding shows the invariance of the crystallite size to the paste fabrication process. The HRTEM investigation reveals that the particles consist of anatase TiO_2 single crystals of regular shape, mostly cubic, terminated by low index planes, *i.e.* {010}, {101}, {112} facets. In particular the HRTEM image in Fig. 3b shows the hexagonal section of one of these nanoparticles imaged along the [111] zone axis, revealing a highly ordered anatase TiO_2 structure. All reflections of the wide-angle X-ray diffraction spectrum in Fig. 3c can be indexed to the anatase phase of TiO_2, with crystal sizes of around 13 nm calculated by the Debye–Scherrer peak width analysis of the

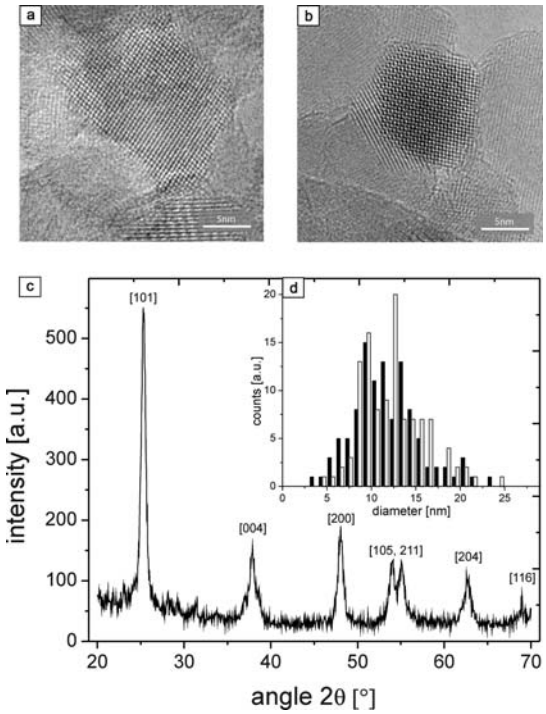

Fig. 3 HRTEM images of mesoporous TiO_2 before (a) and after (b) milling showing that this treatment does not affect crystal size and phase—both particles are identified as anatase TiO_2 viewed along the [111] zone axis. This is also reflected in the crystallite size distributions before (solid) and after (open) film processing extracted from the HRTEM images in (d). All peaks in the XRD spectrum in (c), taken from titania powder before processing, can be indexed to anatase TiO_2.

[101] reflection, which is in good agreement with the HRTEM statistical analysis in Fig. 3d.

Throughout this study the anatase phase was exclusively observed for annealing temperatures up to ~650 °C, while signatures of the rutile phase started to appear at higher temperatures. Structural integrity during the annealing process as shown in Fig. 2 was observed up to the rutile transition. We note that the retention of the porosity and crystallite size up to this temperature is likely a consequence of the carbon scaffold present under anaerobic heating.[8]

A crucial parameter for the efficient functioning of a TiO_2 network in a DSC is the surface area that is accessible for dye adsorption, as photocurrent can only be generated at the dye-sensitised interface. The surface area per volume was measured by nitrogen sorption in calcined TiO_2 before grinding and after manufacture of a film from the ground paste (Fig. 4). Interestingly, the random assembly of the nanocrystals after grinding and processing the material into a film retained the high surface area of the ordered morphology before grinding. This presumably arises from the fact that the surface area is predominately determined by intrinsic nanoporosity of the crystallite assemblies rather than the pores on the mesoscopic length scales generated by the block copolymer assembly (see ESI‡). Beyond retaining the high nanoporosity, the surface area increased during the film manufacture process from 73.4 $m^2\ g^{-1}$ to 80.4 $m^2\ g^{-1}$, reflecting an increase in the accessible surface area to the TiO_2 network caused by the grinding process.

The pore size estimate based on the Barrett–Joyner–Halenda (BJH)[22] method in Fig. 4b supports the previously presented findings for the unground and ground material. While the configuration of TiO_2 nanocrystals in an ordered micellar morphology has a distinct peak in the pore volume at ~28 nm, the pore diameter distribution is much broader for the disordered assembly of the nanocrystals in the processed film.

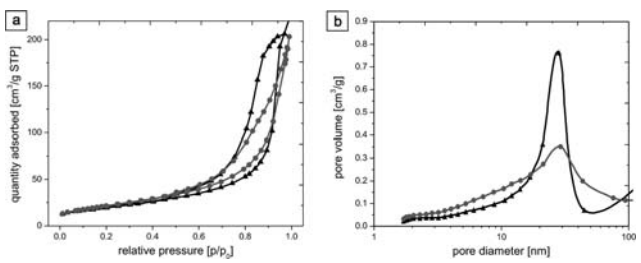

Fig. 4 Nitrogen physisorption data of annealed TiO_2 before (triangles) and after (circles) film processing. (a) Nitrogen adsorption–desorption isotherm, suggesting a total surface area applying the BET method of 73.4 m^2 for the monolith and 80.4 m^2 for the material after grinding and film processing. (b) Pore size distribution as determined by the BJH model for the material before and after grinding. While the configuration of TiO_2 nanocrystals in an ordered micellar morphology results in a characteristic pore size of ~30 nm, the wider distribution of pore size of the material after grinding reflects the more random assembly of the nanocrystals.

2.2 Solar cell performance

A schematic of a DSC is shown in Fig. 5, which illustrates the multifold role of a mesoporous titania film. It determines the internal interface and therefore the sensitization area of the dye and furthermore represents the electron conducting component in the device. Following the photoexcitation of the dye, electrons are injected into the TiO_2, while the dye is regenerated by

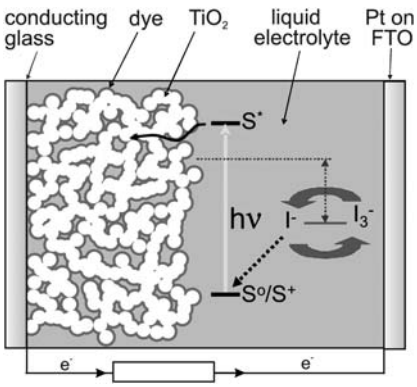

Fig. 5 Schematic presentation of a dye sensitized solar cell incorporating a liquid electrolyte. A highly porous TiO_2 layer on a transparent FTO electrode constitutes the backbone of the cell. After the adsorption of a dye monolayer on the TiO_2 mesostructure, the device is capped by a Pt electrode and filled with a liquid electrolyte. Operation principle: following the photoexcitation of the dye, electrons are injected into the TiO_2. Dye is regenerated by oxidation of the electrolyte, which shuttles the holes to the counter electrode to complete the circuit.

oxidation of the surrounding electrolyte, which shuttles the holes to the counter electrode to complete the circuit.

Following the fabrication of mesoporous TiO_2 films through the presented monolithic route, liquid electrolyte DSCs were fabricated as described in the experimental section.

2.2.1 Thickness dependence of DSC operation. Fig. 6 shows the performance of the solar cells incorporating a range of TiO_2 film thicknesses of 3.5 μm and 9 μm. From a mechanical viewpoint, fabricating robust up to 17 μm thick mesoporous films from normal nanoparticles has recently represented a breakthrough in titania paste fabrication.[17] Here, our films remain robust and crack free to thicknesses over 30 μm, in stark contrast to films fabricated directly using copolymer structure-directed sol–gel chemistries, where the single layer thickness is limited to less than one micrometre.[9,23] This entirely overcomes the issue of volume reduction, stress, and delamination in polymer directed, self-assembled films. In Fig. 6a the spectral response is shown for solar cells incorporating our TiO_2 films of 3.5 μm and 9 μm in thickness. The EQE peaks are similar, around 70% at 525 nm. The action spectra of the 9 μm thick film is broader, due to the longer optical path lengths in the thicker cell, leading to more absorbed light by the dye at wavelengths longer than 600 nm.

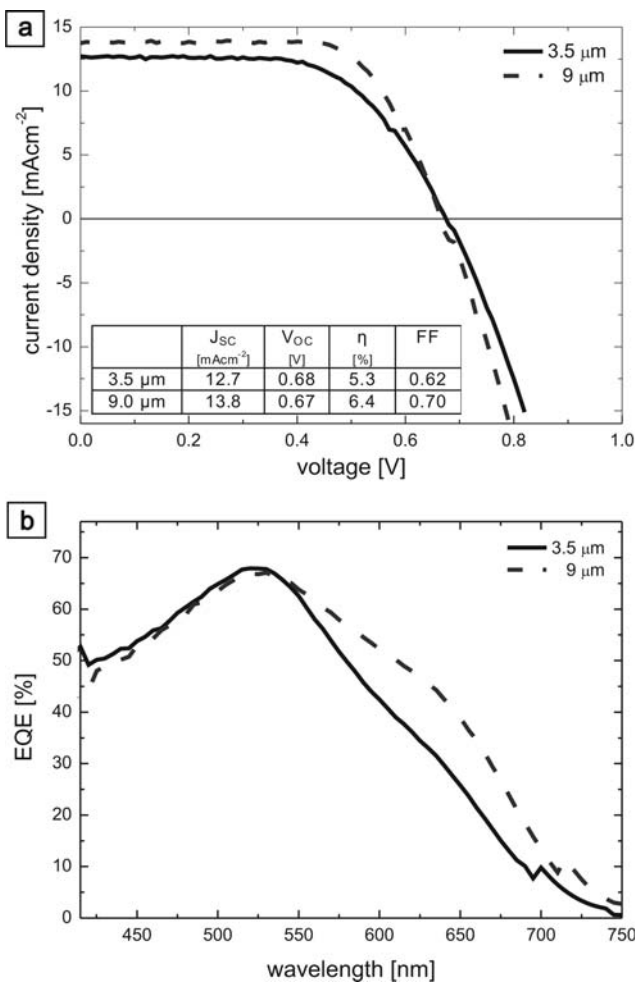

	J_{SC} [mAcm^{-2}]	V_{OC} [V]	η [%]	FF
3.5 μm	12.7	0.68	5.3	0.62
9.0 μm	13.8	0.67	6.4	0.70

Fig. 6 Liquid electrolyte dye sensitized solar cell performance. (a) EQE, and (b) current–voltage characteristics for devices that include mesoporous TiO_2 layers of 3.5 μm (solid line) and 9 μm (dashed lined). The inset table summarises the key photovoltaic properties of the cells.

In Fig. 6b the current–voltage characteristics are shown for solar cells measured under AM 1.5 simulated sunlight. The 9 μm thick film gave a power conversion efficiency of 6.4%. For thicker films we did not observe an increase in power conversion efficiency. For example, a 30 μm thick layer exhibited a current of only 7.6 mA cm^{-2}, accompanied by a fill factor of 0.34, resulting in an overall efficiency of only 2%. To understand this behaviour, we have probed the transport and recombination in these DSCs *via* transient photocurrent and photovoltage decay measurements under constant current short-circuit conditions. From these measurements we estimate an electron diffusion length of 17 μm. All these data are shown in the ESI.‡ We therefore attribute insufficient charge carrier transport properties to the limited performance of extremely thick films. Scanning from short-circuit towards open-circuit results in an increased charge density in the device due to the reduced current collection. This causes an increase in the recombination rate, however it has been observed that the charge collection rate in dye-sensitized solar cells does not increase comparably when applying a forward bias to the solar cell, implying that there is a reduction in the diffusion length under working conditions.[24,25] This would justify why the fill factor also reduces for the 30 μm thick films where poor current collection is limiting the device performance.

We note that the illumination intensity of our spectral response measuring unit is extremely low (~0.1 mW cm^{-2}) and the illumination spot is much smaller than the active area of the device (~1 mm^2 spot size on a *ca.* 0.31 cm^2 device), resulting in a lower current compared to measurements under simulated sunlight.

The standard liquid-electrolyte based DSC which employs sintered colloidal nanoparticles works most efficiently with active layers up to ~20 μm thickness.[26] In our case, excellent performance was already achieved for 3.5 μm thick films. In Fig. 7a, the current–voltage characteristics for our best 3.5 μm thick cell are shown under simulated AM 1.5 full sunlight (100 mW cm^{-2}) and low light intensity (21 mW cm^{-2}). This device exhibited a power conversion efficiency of 6.44% under full sun conditions. The main difference from the results presented in Fig. 6b is a slightly improved open-circuit voltage and fill factor. Under low light levels of 21 mW cm^{-2} we observe an even more impressive power conversion efficiency of 8.1%. The photocurrent increases linearly with intensity over this range, but the fill factor increases considerably as the intensity is reduced, accounting for the overall enhanced performance. We note that these devices are fabricated with a non-volatile electrolyte (Robust) and a standard ruthenium complex (N719), and these results for thin films represent a significant improvement upon the state-of-the-art.

2.2.2 Light scattering. Light scattering plays an important role in enhancing the efficiency of DSCs because it increases the effective optical path length in the active medium, which is especially significant for the enhancement of light absorption near the absorption onset where the extinction coefficient is low.[27] This is particularly effective for TiO_2-based solar cells since the high refractive index of TiO_2 results in the scattered light being predominantly confined within the TiO_2 layer. For record-efficiency DSCs, large titania particles of around 200–

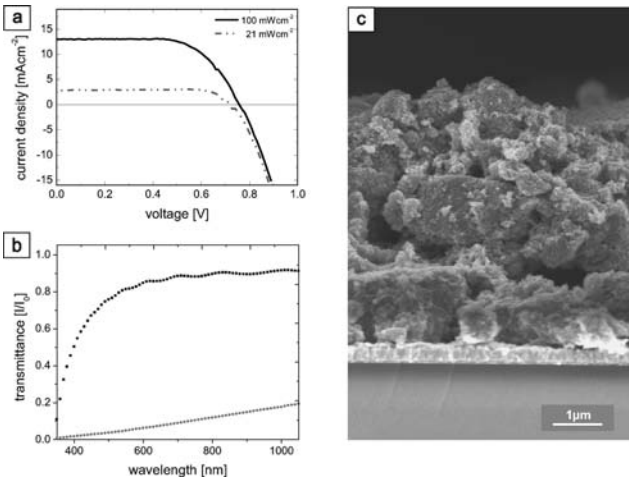

Fig. 7 Top performance of a DSC prepared by the monolithic route for a 3.5 μm thick film: (a) current–voltage characteristics for a 3.5 μm thick DSC under simulated AM 1.5 full sunlight (100 mW cm^{-2}) and low light intensity (21 mW cm^{-2}). (b) The pronounced scattering properties are revealed in the UV-vis transmittance spectrum (circles) compared to a conventional nanoparticle film (squares). (c) Cross-sectional SEM image, showing roughness on the μm length scale.

400 nm in diameter are added to the normal particles (20 nm).[28] This is clearly advantageous, but the large particles have a low surface area and exhibit poor dye uptake. High performance cells therefore typically consist of two layers—a transparent nanoparticle layer and an opaque layer of large scattering particles. To meet scattering and light absorption requirements in such a cell, the double layer titania film has to be rather thick, which sacrifices open-circuit voltage and fill factor.[17,29,30]

The fabrication approach presented in this study gives rise to a TiO_2 film structure which inherently combines a high internal surface area with the strong scattering of light. In Fig. 7c, a side view of a 3.5 μm thick film is presented. The basic film constituents, titania nanocrystallites, typically agglomerate into building blocks on the micrometre scale which has the fortunate effect of uniting scattering and light absorption in a single, thin layer.

The scattering abilities of our titania film structures are compared to light transmission through a conventional titania film of 20 nm sized particles in Fig. 7b. Already a 1.5 μm thick film fabricated from our mesoporous TiO_2 paste results in multiple scattering of the incoming light while the standard film fabricated from sintered 20 nm sized colloidal nanoparticles is almost transparent to visible light. We attribute the scattering properties a key role for the excellent functioning of our thin films.

3 Conclusion

In summary, we have developed a protocol for fabricating up to 30 μm thick mesoporous TiO_2 films. In contrast to standard DSC assembly in which commercially manufactured TiO_2 nanoparticles are used, we have employed sol–gel chemistry in the presence of structure-directing diblock copolymers for TiO_2 nano-particle synthesis. While the material initially assumes a micellar structure that is dictated by block copolymer self-assembly, this self-assembled structure is lost upon further processing. However, the compartmentalization of the sol–gel chemistry by the micellar copolymer morphology enables the full control of a number of parameters controlling the DSC device performance, such as the crystal size, overall crystallinity and nanoparticle surface structure.[31] Further, the separation of mesopore formation and crystallization from thin film fabrication renders this process highly suitable to up-scale to large area coating technologies. Films made from nanoparticle pastes are highly porous and the assembly of TiO_2 into a highly heterogeneous structure combines very high light absorption with substantial light scattering, making them ideally suited for incorporation into the active layer of dye-sensitized solar cells. A solar to electrical power conversion efficiency of over 6.4% was obtained for DSCs incorporating 3.5 μm thick films measured under full sun conditions (AM 1.5 (100 mW cm^{-2})). Under lower light levels of 21 mW cm^{-2} this efficiency increases to over 8%. The separate control of TiO_2 crystal morphology and device mesostructure demonstrates that soft self-assembled templates can yield great control over both inorganic and organic aspects of the DSC, resulting in advantageous optical and electronic functionality. In addition, this procedure is applicable to a large number of mesoporous materials which can be fabricated employing structure-directing agents for a broad range of applications.

4 Experimental

4.1 Monolith fabrication

Mesoporous TiO_2 was prepared as described previously by Lee *et al.*[8] Poly(isoprene-*b*-ethylene oxide) (PI-*b*-PEO) with a molecular weight of $M_n = 33.5$ kg mol^{-1}, polydispersity of 1.1, 23 wt% PEO was dissolved in anhydrous THF, mixed with titanium isopropoxide and $TiCl_4$ of equal molarity in the ratio of 1 : 1.5 by mass and stirred for at least 2 h. The solution was placed on a hot plate at 50 °C for more than 24 h to slowly evaporate the solvent, then in a vacuum oven at 130 °C to completely remove the residual solvent. To convert the titania precursor into TiO_2, the material was transferred into a tube furnace for high temperature processing at 525 °C for 2 h under an inert atmosphere with a ramping rate of 1 °C min^{-1}. During this process, PI was transformed into an amorphous graphitic carbon material acting as a scaffold supporting the pore walls and thereby preventing pore collapse.[8] The carbon was then removed by heating the material to 500 °C for 5 h under O_2.

4.2 Paste fabrication

After cooling, the mesoporous TiO_2 monolith was ground in a mortar until a fine powder was obtained. This TiO_2 powder was incorporated into a paste closely following the recipe of Ito *et al.*[17] The powder (222 mg) was mixed with acetic acid (0.04 ml), water (0.2 ml), and ethanol (0.66 ml), with the solvents added drop-wise. The solvent/powder mix was ground until all excess solvent was incorporated or had evaporated. The mixture was transferred into a large vial with excess ethanol (4 ml), mixed with α-terpineol (0.8 g) and sonicated with an ultrasonic horn for 15 min (2 min work + 2 min rest). Ethyl cellulose (0.12 g, viscosity: 30–60 mPa s), 5% in toluene–ethanol 80 : 20 vol : vol

was added and stirred at room temperature for about 15 min, followed by sonication for 15 min (2 min work + 2 min rest). The paste was concentrated by evaporation of the ethanol at room temperature in an open beaker.

4.3 Material characterization

Imaging characterisation of mesoporous TiO_2 was carried out by scanning electron microscopy (SEM) on a LEO Ultra 55 at an acceleration voltage of 5 kV as well as by transmission electron microscopy (TEM) on a FEI Tecnai T-12 TWIN TEM at an acceleration voltage of 200 kV. Furthermore, high resolution transmission electron microscopy (HRTEM) using a JEOL 4000EX microscope was employed with 400 kV acceleration voltage and a point resolution of 0.17 nm. Wide-angle X-ray diffraction scans were taken with a Philips PW1830 Generator 3. Surface area and pore characterisation was accomplished through nitrogen physisorption with a Micromeritics TriStar 3000 (saturation pressure of 745 mmHg). Small-angle X-ray (SAXS) characterisation was carried out in transmission geometry, using a Nanostar camera (Bruker AXS, Karlsruhe, Germany), with Cu-Kα radiation ($\lambda = 0.154$ nm) and a sample-to-detector distance of 1.05 m. See ESI‡f or further experimental and modelling details.

4.4 Solar cell assembly

Fluorine doped SnO_2 (FTO) coated glass sheets (Nipon Sheet Glass, TEC15) were manually cleaned with Hellmanex soap, acetone, and isopropanol followed by 10 min in an O_2 plasma etcher. The mesoporous TiO_2 pastes were applied by doctor-blading: two parallel strips of Scotch tape were adhered to the edge of the FTO sheets to control the height of the doctor-blade. The paste was dispensed at one end of the glass sheet, with a cylindrical glass pipette used as the doctor blade, which was manually translated along the Scotch tape strips, thereby coating the entire substrate. A doctor blade height of one Scotch tape ($\sim$50 μm) gave approximately 1–1.5 μm thick dry films. For thicker films up to three Scotch tapes were used on top of each other. The coated sheets were dried in air at 50 °C until the solvent had completely evaporated, then at 100 °C for 5 min followed by 10 min at 150 °C. For thicker films this process was applied repeatedly. The samples were slowly heated on a hot plate to 350 °C for 30 min to burn off the ethyl cellulose, then at 500 °C for 1 h under O_2 to ensure good interconnection between the particles. The samples were soaked in a 40 mM $TiCl_4$ solution at 80 °C for 30 min. The films were then cleaned in Millipore water, dried and heated to 500 °C for 30 min in air. They were cooled to 80 °C before immersion in a 0.5 mM solution of *cis*-di(thiocyanato)-bis(2,2′-bipyridyl-4-carboxylate-4′-carboxylic acid)-ruthenium(II) (termed N719) in a mixture of acetonitrile–*tert*-butyl alcohol (volume ratio 1 : 1) and kept in the dark overnight at room temperature.

The counter electrodes used for these devices were sheets of pre-drilled platinized FTO glass. The platinization was performed by coating the FTO with hexachloroplatinic (IV) acid from an anhydrous isopropanol solution (50 mM) followed by heating to 450 °C for 15 min. The dyed TiO_2 electrodes were washed in acetonitrile, dried and assembled in a sandwich type cell configuration with the platinized counter electrodes, using a 'hot-melt' 50 μm thick surlyn spacer (Dupont) to seal the working and counter electrodes together. A drop of 'Robust' liquid electrolyte (0.8 M PMII, 0.15 M iodine, 0.1 M GuNCS, and 0.5 M NMBI in 3-methoxypropionitrile)[32] was dispensed on to the hole in the counter electrode and the cell was filled *via* vacuum back-filling[33] and sealed with polyimide tape (Dupont). For light scattering experiments, reference titania films of standard nanoparticle paste (Dyesol, 18NR-T) were similarly deposited by doctor blading.

4.5 Solar cell characterisation

The solar cells were measured under AM 1.5 simulated sunlight generated by a 300 W Oriel solar simulator using AM 0 and AM 1.5 filters. The power of the simulated light was measured using a calibrated Si photo diode (Fraunhofer Institute for Solar Energy Systems). The mismatch factor to the solar spectrum was calculated over the entire spectral responsive region of both the test solar cells and calibration diode following the method of Seaman.[34] The active area of the DSCs was defined by a black optical mask to 0.13 cm^2. For the external quantum efficiency (EQE) measurements the cell was illuminated by a spectrally resolved halogen lamp and the intensity was measured by the calibrated Si diode. The cells were illuminated from the FTO side at an approximate intensity of 0.1 mW cm^{-2} at each wavelength interval, with an illumination spot size of approximately 1 mm^2. The current–voltage measurements were recorded by a Keithley 237 sourcemeter connected to a computer.

Acknowledgements

M.N., S.H., and U.S. acknowledge the European RTN-6 Network "Polyfilm" and S.H. acknowledges a scholarship of the Bayerische Graduiertenförderung. C.D. acknowledges the Royal Society for Funding. This work was funded in part by the EPSRC Nanotechnology Grand Challenges: Energy grant (EP/F056702/1), the Department of Energy (DE-FG02 87ER45298) through the Cornell Fuel Cell Institute (CFCI), the National Science Foundation (DMR-0605856), and the Cornell Universiy KAUST Center for Research and Education. The sabbatical leaves of U.W. was supported by the Leverhulme Trust and EPSRC. We thank Mathias Kolle for help with Fig. 1 and Richard Friend for valuable discussions and support.

References

1 B. O'Regan and M. Grätzel, *Nature*, 1991, **353**, 737–740.
2 M. Nazeeruddin, P. Pechy, T. Renouard, S. Zakeeruddin, R. Humphry-Baker, P. Comte, P. Liska, L. Cevey, E. Costa, V. Shklover, L. Spiccia, G. Deacon, C. Bignozzi and M. Gratzel, *J. Am. Chem. Soc.*, 2001, **123**, 1613–1624.
3 M. Gratzel, *J. Photochem. Photobiol., A*, 2004, **164**, 3–14.
4 T. Thurn-Albrecht, J. Schotter, C. Kastle, N. Emley, T. Shibauchi, L. Krusin-Elbaum, K. Guarini, C. Black, M. Tuominen and T. Russell, *Science*, 2000, **290**, 2126–2129.
5 E. J. W. Crossland, S. Ludwigs, M. A. Hillmyer and U. Steiner, *Soft Matter*, 2007, **3**, 94–98.
6 P. Yang, D. Zhao, D. Margolese, B. Chmelka and G. Stucky, *Nature*, 1998, **396**, 152–155.
7 M. Templin, A. Franck, A. DuChesne, H. Leist, Y. Zhang, R. Ulrich, V. Schadler and U. Wiesner, *Science*, 1997, **278**, 1795–1798.

8 J. Lee, M. C. Orilall, S. C. Warren, M. Kamperman, F. J. Disalvo and U. Wiesner, *Nat. Mater.*, 2008, **7**, 222–228.
9 M. Zukalova, A. Zukal, L. Kavan, M. Nazeeruddin, P. Liska and M. Grätzel, *Nano Lett.*, 2005, **5**, 1789–1792.
10 M. Wei, Y. Konishi, H. Zhou, M. Yanagida, H. Sugihara and H. Arakawa, *J. Mater. Chem.*, 2006, **16**, 1287–1293.
11 Dina Fattakhova-Rohlfing, Michael Wark, Torsten Brezesinski, Bernd M. Smarsly and Jiri Rathousky, *Adv. Funct. Mater.*, 2007, **17**, 123–132.
12 J. M. Szeifert, D. Fattakhova-Rohlfing, D. Georgiadou, V. Kalousek, J. Rathousky, D. Kuang, S. Wenger, S. M. Zakeeruddin, M. Graetzel and T. Bein, *Chem. Mater.*, 2009, **21**, 1260–1265.
13 P. Simon, R. Ulrich, H. Spiess and U. Wiesner, *Chem. Mater.*, 2001, **13**, 3464–3486.
14 A. Finnefrock, R. Ulrich, G. Toombes, S. Gruner and U. Wiesner, *J. Am. Chem. Soc.*, 2003, **125**, 13084–13093.
15 M. Nedelcu, J. Lee, E. J. W. Crossland, S. C. Warren, M. C. Orilall, S. Guldin, S. Huettner, C. Ducati, D. Eder, U. Wiesner, U. Steiner and H. J. Snaith, *Soft Matter*, 2009, **5**, 134–139.
16 E. J. W. Crossland, M. Kamperman, M. Nedelcu, C. Ducati, U. Wiesner, D. M. Smilgies, G. E. S. Toombes, M. A. Hillmyer, S. Ludwigs, U. Steiner and H. J. Snaith, *Nano Lett.*, 2009, **9**, 2807–2812.
17 S. Ito, P. Chen, P. Comte, M. K. Nazeeruddin, P. Liska, P. Pechy and M. Grätzel, *Progr. Photovolt.: Res. Appl.*, 2007, **15**, 603–612.
18 O. F. Gobel, M. Nedelcu and U. Steiner, *Adv. Funct. Mater.*, 2007, **17**, 1131–1136.
19 F. Zernike and J. Prins, *Z. Phys.*, 1927, **41**, 184–194.
20 P. Debye and A. Bueche, *J. Appl. Phys.*, 1949, **20**, 518–525.
21 P. Debye, H. Anderson and H. Brumberger, *J. Appl. Phys.*, 1957, **28**, 679–683.
22 E. Barrett, L. Joyner and P. Halenda, *J. Am. Chem. Soc.*, 1951, **73**, 373–380.
23 J. Prochazka, L. Kavan, V. Shklover, M. Zukalova, O. Frank, M. Kalbac, A. Zukal, H. Pelouchova, P. Janda, K. Week, M. Klementova and D. Carbone, *Chem. Mater.*, 2008, **20**, 2985–2993.
24 J. Nissfolk, K. Fredin, A. Hagfeldt and G. Boschloo, *J. Phys. Chem. B*, 2006, **110**, 22950.
25 H. J. Snaith, R. Humphry-Baker, P. Chen, I. Cesar, S. M. Zakeeruddin and M. Graetzel, *Nanotechnology*, 2008, **19**, 424003.
26 H. J. Snaith and L. Schmidt-Mende, *Adv. Mater.*, 2007, **19**, 3187–3200.
27 C. Barbe, F. Arendse, P. Comte, M. Jirousek, F. Lenzmann, V. Shklover and M. Gratzel, *J. Am. Ceram. Soc.*, 1997, **80**, 3157–3171.
28 S. Ito, P. Liska, P. Comte, R. Charvet, P. Pechy, U. Bach, L. Schmidt-Mende, S. Zakeeruddin, A. Kay, M. Nazeeruddin and M. Gratzel, *Chem. Commun.*, 2005, 4351–4353.
29 S. Ito, S. Zakeeruddin, R. Humphry-Baker, P. Liska, R. Charvet, P. Comte, M. Nazeeruddin, P. Pechy, M. Takata, H. Miura, S. Uchida and M. Gratzel, *Adv. Mater.*, 2006, **18**, 1202.
30 H. J. Snaith, L. Schmidt-Mende, M. Gratzel and M. Chiesa, *Phys. Rev. B: Condens. Matter Mater. Phys.*, 2006, **74**, 045306.
31 S. Guldin *et al.*, in preparation.
32 D. Kuang, S. Ito, B. Wenger, C. Klein, J. Moser, R. Humphry-Baker, S. Zakeeruddin and M. Gratzel, *J. Am. Chem. Soc.*, 2006, **128**, 4146–4154.
33 H. Han, U. Bach, Y.-B. Cheng and R. A. Caruso, *Appl. Phys. Lett.*, 2007, **90**, 213510.
34 C. Seaman, *Sol. Energy*, 1982, **29**, 291–298.

